PHASE-FIELD MODEL FOR DEGRADATION OF STEEL FIBER-REINFORCED ULTRA-HIGH PERFORMANCE CONCRETE DURING LOW CYCLE FATIGUE

M. PISE[∗]**, J. SCHRÖDER**[∗]**, D. BRANDS**[∗]**, G. GEBUHR**[†] **AND S. ANDERS**[†]

[∗] Institute of Mechanics, Department of Civil Engineering, Faculty of Engineering,
University of Duisburg-Essen, Essen, Germany
e-mail: mangesh.pise@uni-due.de, j.schroeder@uni-due.de, dominik.brands@uni-due.de,

[†] Chair for Construction Materials, Faculty of Architecture and Civil Engineering,
Bergische Universität Wuppertal, Wuppertal, Germany
e-mail: gebuhr@uni-wuppertal.de, s.anders@uni-wuppertal.de

Key words: Phase-field Model For Fracture, Steel Fiber Reinforced Concrete, Ultra High Performance Concrete, Low Cycle Fatigue

Abstract. The degradation of fiber-reinforced ultra-high performance concrete (UHPC) is mainly dominated by the pseudo-ductile behavior of concrete material and the complex fiber-matrix interactions. A phenomenological material model is derived, which is a combination of the superposed models of one-dimensional elasto-plasticity to describe the fibers and an elasto-plastic phase-field model of fracture in concrete material. Therein, to capture the distinct behavior of concrete in tension and compression, two different continuous stepwise linearly approximated degradation functions are constructed. The uniaxial tensile and compression tests are simulated to calibrate the material parameters of UHPC. Three-point bending beam tests at low cycles are simulated to study the failure behavior of reinforced UHPCs with different fiber contents and orientations. The volume fraction of fibers and orientation distribution functions (ODF) incorporate various contents and directions of reinforced fibers. The simulated results and experimental data are plotted in terms of load-crack mouth opening displacement (CMOD) curves and compared with each other to check the capabilities of the presented model. The calculated and interpolated residual-COMD curves using numerical and experimental results are compared to validate the accuracy of the simulated results in terms of the degradation of the stiffness and plastic part of the crack opening during failure.

1 INTRODUCTION

In the last decade, the newly developed ultra-high performance concrete (UHPC) has become popular as a construction material because of its properties like high strength and outstanding durability compared to standard concrete. However, UHPC can not be used in pure form to build the structures subjected to dynamic loading because it exhibits low tensile strength and highly brittle behavior, see [2, 8]. The higher ductility of UHPC can be achieved by adding steel fibers, see [1, 21]. These fibers improve the strain-hardening properties of UHPC, which increases load-bearing capacity even during cyclic loading. This phenomenon occurs because of the transfer of the stresses from cracked concrete matrix to fibers which restrain the further growth of cracks. Hence, the failure behavior of fiber-reinforced UHPC is highly influenced by the quantity, distribution, and ori-

entations of fibers. Many numerical models are developed to analyze the complex nonlinear characteristics of concrete during failure, e.g., see [3,10,11,20,22]. However, there is a lack of complete knowledge about the complex failure process of fiber-reinforced UHPC under cyclic loading. Therefore, the intense research is focused on the experimental and numerical analysis of the failure of HPC and UHPC under fatigue within the German Research Foundation Priority Programme 2020 (DFG SPP 2020). In SPP 2020, the authors of this contribution have a joint project to work on the mentioned tasks.

This contribution aims to develop an elasto-plastic phase-field model to analyze the failure of reinforced UHPC subjected to cyclic loading. The focus is on the failure analysis of reinforced UHPC beams with different fiber contents and orientations. At first, the failure behavior under low-cycle fatigue is investigated on three-point bending beams. The detailed experimental procedure with the used composition of UHPC and experimental results are documented in Section 2. Furthermore, the constitutive framework containing superposed energy functions of one-dimensional elasto-plasticity for the fibers and an elasto-plastic phase-field model of fracture in concrete material is presented in section 3. The non-associative Drucker-Prager yield criterion for the UHPC phase and the one-dimensional von Mises elasto-plasticity for the fibers are considered, cf. [9]. In section 4, the numerical model is first calibrated by simulating the uniaxial tensile and compression tests for pure UHPC. Subsequently, three-point bending beam tests for UHPC, using different fiber contents and orientations, are simulated. The simulation results are then compared with experimental data, and the impact of varying fiber contents and orientations of embedded steel fibers is thoroughly analyzed. Furthermore, the values of residual stiffness are calculated for each loading cycle using experimental and numerical results and compared with each other to validate the prediction capability of the presented model. Finally, the presented work is concluded in Section 5.

2 Experimental program

The flexural tests on reinforced UHPC using the smooth steel microfibres are performed, cf. [8], to understand the material behavior of reinforced UHPC and provide the basis for calibrating the numerical model presented in this contribution. The components used to prepare the UHPC mixture are given in Table 1.

Table 1: Components of the UHPC mixture.

| Component	Quantity in kg/m³
CEM I 52, 5R	795
Quartz powder	198
Quartz sand	971
Superplasticizer	24
Microsilica	169
Water	188
Fibers	0/57/115

The experiments utilize notched beams having dimensions of 150 x 150 x 700 mm³ according to DIN EN 14561. The applied force and CMOD are measured during the tests. Linear Variable Differential Transformer (LVDT) fixed at the level of the lower edge of the specimen, as shown in the experimental setup in Fig. 1, are used to measure the value of CMOD.
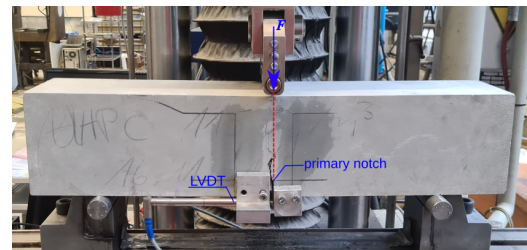
Figure 1: Experimental setup for the three-point bending beam tests.

The fibers added in the UHPC have a length of 13 mm and a diameter of 0.19 mm are depicted in Fig. 2a. UHPC beams with fiber contents of 0/57/115 kg/m³, i.e., 0/0.75/1.5 vol. %, are used for the investigations. The reference concrete mixture – developed within the Priority Programme 2020 (SPP 2020) of the German Research Foundation (DFG) – is used for the tests, which is ex-

tensively researched in other works, e.g. see [6,13]. Fig. 2b shows the embedded microfibers in a damaged part of the UHPC bending beam during experiment.

(a)

(b)
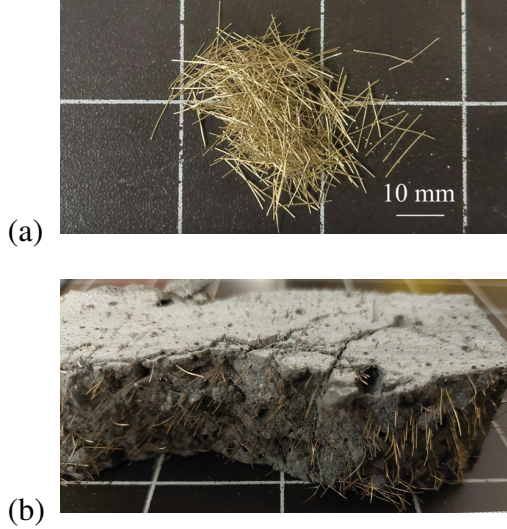
Figure 2: Smooth steel microfibers: (a) loose sample and (b) embedded in a cut section of the damaged part of a UHPC bending beam.

Throughout the test, periodic unloading cycles were carried out as shown schematically in Fig. 3 depicting the idealized force-crack opening curve.
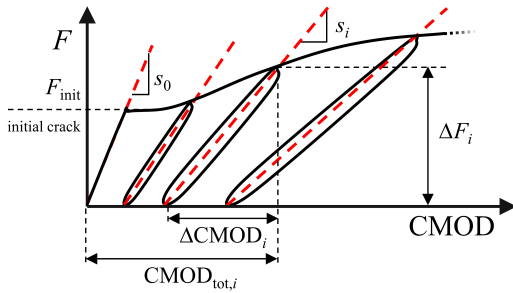
Figure 3: Schematic representation of the force-CMOD curve of the tests carried out and parameters used to calculate the secant modulus (residual stiffness), adopted from [9] and [18].

This loading scheme is used to investigate the initial stiffness s_0 and residual stiffness s_i of the test specimens as a gradient modulus for specific crack openings. The stiffness is determined based on RILEM (1990), i.e.,

$$s_i = \frac{\Delta F_i}{\text{CMOD}_{\text{el},i}}, \qquad (1)$$

where ΔF_i refers to the difference between the associated forces and $\text{CMOD}_{\text{el},i}$ corresponds to the crack mouth opening difference between the reversal point and the intersection of the loading-unloading branch of the load-CMOD curve, i.e.,

$$\text{CMOD}_{\text{el},i} = \text{CMOD}_{\text{tot},i} - \text{CMOD}_{\text{pl},i} . \qquad (2)$$

Figs. 3a and b show the exemplary load–CMOD curves for fiber reinforced UHPC with a fiber content of 57 kg/m^3 and the evolution of the residual stiffness for all the performed experiments, respectively. The strain hardening behavior is observed in the experiments. Hence, the overall load-bearing capacity of the beams continue to increase accordingly once the level of proportionality was reached.

(a)

(b)
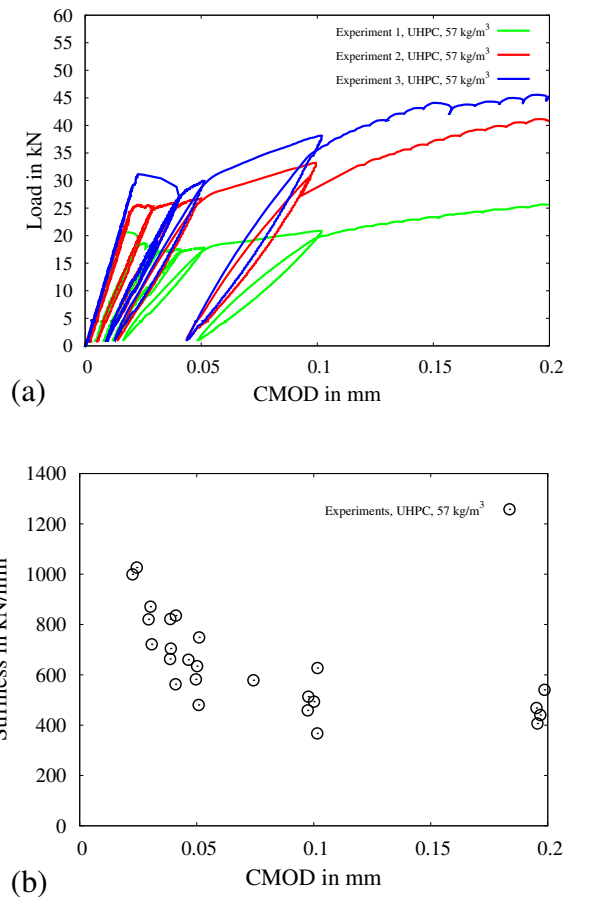
Figure 4: Three-point bending beam low-cycle tests: (a) exemplary load–CMOD-curves for fiber-reinforced UHPC with fiber content of 57 kg/m^3 and (b) evolution of residual stiffness.

3

3 Constitutive model

Here, the phenomenological material model, developed in our recent works [9, 16], is used for the analysis of failure of fiber-reinforced UHPC. Therein, two different phases for UHPC matrix and embedded fibers are considered. The stored energy function per unit volume ψ is defined as

$$\psi = \mathrm{v}^{\mathrm{UHPC}}\,\psi^{\mathrm{UHPC}} + \mathrm{v}^{\mathrm{F}}\,\psi^{\mathrm{F}}\,, \qquad (3)$$

where the volume fraction $\mathrm{v}^{\mathrm{UHPC}}$ of UHPC phase and volume fraction v^{F} of fiber are conserved by the condition $\mathrm{v}^{\mathrm{UHPC}} = 1 - \mathrm{v}^{\mathrm{F}}$. An energy function ψ^{UHPC} for UHPC phase reads

$$
\begin{aligned}
\psi^{\mathrm{UHPC}} =\ & g(q)\left[\psi_0^{\mathrm{e+,UHPC}} + \psi_0^{\mathrm{p,UHPC}}\right] \\
& + \psi_0^{\mathrm{e-,UHPC}} + (1 - g(q))\,\psi^{\mathrm{c,UHPC}} \\
& + \frac{2\,\psi^c l}{\zeta}\left[\tfrac{1}{2l}\,q^2 + \tfrac{l}{2}\,||\nabla q||^2\right]\,,
\end{aligned}
\qquad (4)
$$

where l is the length scale parameter and ∇q is a gradient of the phase-field parameter $\bar{q} \in [0,1]$, which describes the damage in UHPC phase. The parameter ζ controls the speed of evolution of phase-field parameter q. Two different parameters for the critical fracture energy in tension $\psi^{\mathrm{c,UHPC}} = \psi_{\mathrm{t}}^{\mathrm{c,UHPC}}$ and in compression $\psi^{\mathrm{c,UHPC}} = \psi_{\mathrm{c}}^{\mathrm{c,UHPC}}$ are implemented, see [19]. The values of these critical fracture energies are calibrated according to the values of tensile strength f_{t} and compressive strength f_{c} of UHPC, see [18]. A positive $\psi_0^{\mathrm{e+}}(\varepsilon^{\mathrm{e,UHPC}})$ and a negative $\psi_0^{\mathrm{e-}}(\varepsilon^{\mathrm{e,UHPC}})$ reference elastic energies for UHPC phase, cf. [5], read

$$
\begin{aligned}
\psi_0^{\mathrm{e+,UHPC}} =\ & \kappa\langle\mathrm{tr}[\varepsilon^{\mathrm{e,UHPC}}]\rangle_+^2/2 \\
& + \mu||\mathrm{dev}\,\varepsilon^{\mathrm{e,UHPC}}||^2\,, \\
\psi_0^{\mathrm{e-,UHPC}} =\ & \kappa\langle\mathrm{tr}[\varepsilon^{\mathrm{e,UHPC}}]\rangle_-^2/2\,,
\end{aligned}
\qquad (5)
$$

where μ and κ are the Lamé coefficients of UHPC phase and Macaulay's notation describes the operator $\langle\bullet\rangle_\pm = 1/2\,(\,\bullet\pm|\,\bullet\,|\,)$. The elastic strains $\varepsilon^{\mathrm{e,UHPC}} := \varepsilon - \varepsilon^{\mathrm{p,UHPC}}$ in UHPC phase is calculated using the plastic strains $\varepsilon^{\mathrm{p,UHPC}}$ in UHPC phase and the total strain tensor ε.

A plastic energy $\psi^{\mathrm{p,UHPC}}$ for UHPC phase is given as

$$\psi^{\mathrm{p,UHPC}} = g(q)\,\psi_0^{\mathrm{p,UHPC}}\,, \qquad \text{with}$$

$$\psi_0^{\mathrm{p,UHPC}} = y_0^{\mathrm{UHPC}}\alpha^{\mathrm{UHPC}} + \frac{h^{\mathrm{UHPC}}}{2}\alpha^{\mathrm{UHPC}2} \qquad (6)$$

where α^{UHPC}, y_0^{UHPC} and h^{UHPC} denote the equivalent plastic strain, yield stress and hardening parameter for UHPC phase, respectively.

The energy function ψ^{F} for fiber is constructed considering the one-dimensional elasto-plasticity problem for the embedded steel fibers with a preferred direction $\boldsymbol{a}$ where $||\boldsymbol{a}|| = 1$, reads

$$\psi^{\mathrm{F}} = \psi^{\mathrm{e,F}}\left(\boldsymbol{\varepsilon}, \mathbf{M}, e^{\mathrm{p,F}}\right) + \psi^{\mathrm{p,F}}\left(\alpha^{\mathrm{F}}\right)\,. \qquad (7)$$

The related equation for an elastic strain $e^{\mathrm{e,F}}$ and a plastic strain $e^{\mathrm{p,F}}$ in fiber using the total strain e^{F} for fiber can be written as

$$e^{\mathrm{e,F}} = e^{\mathrm{F}} - e^{\mathrm{p,F}} \quad \text{with} \quad e^{\mathrm{F}} = \boldsymbol{\varepsilon}:\mathbf{M}\,, \qquad (8)$$

where the structural tensor $\mathbf{M} := \boldsymbol{a}\otimes\boldsymbol{a}$ is used to mapped the material behavior of fibers on a preferred fiber direction $\boldsymbol{a}$ in the three-dimensional domain, cf. [7]. The considered elastic $\psi^{\mathrm{e,F}}$ and plastic $\psi^{\mathrm{p,F}}$ energy functions read

$$\psi^{\mathrm{e,F}}\left(\boldsymbol{\varepsilon}, \mathbf{M}, e^{\mathrm{p,F}}\right) = \tfrac{1}{2}\,E^{\mathrm{F}}\left(e^{\mathrm{F}} - e^{\mathrm{p,F}}\right)^2$$

$$\text{and} \quad \psi^{\mathrm{p,F}}\left(\alpha^{\mathrm{F}}\right) = y_0^{\mathrm{F}}\,\alpha^{\mathrm{F}} + \tfrac{1}{2}\,h^{\mathrm{F}}\,\alpha^{\mathrm{F}2}\,, \qquad (9)$$

where the elastic moduli E^{F}, the initial yield stress y_0^{F} and the hardening parameter h^{F} are considered for fiber. An additively constructed structure of the total stress tensor $\boldsymbol{\sigma}$ which is used in the momentum balance equation, reads

$$\boldsymbol{\sigma} := \mathrm{v}^{\mathrm{UHPC}}\,\boldsymbol{\sigma}^{\mathrm{UHPC}} + \mathrm{v}^{\mathrm{F}}\,\boldsymbol{\sigma}^{\mathrm{F}}\,. \qquad (10)$$

The stress tensor $\boldsymbol{\sigma}^{\mathrm{UHPC}}$ for UHPC phase is derived using the energy function for UHPC phase ψ^{UHPC}, see Eq. (4), reads

$$
\begin{aligned}
\boldsymbol{\sigma}^{\mathrm{UHPC}} =\ & g^\pm(q)\,\kappa^{\mathrm{UHPC}}\langle\mathrm{tr}\,\boldsymbol{\varepsilon}^{\mathrm{e,UHPC}}\rangle_+\mathbf{I} \\
& + g^\pm(q)\,2\,\mu^{\mathrm{UHPC}}\,\mathrm{dev}\boldsymbol{\varepsilon}^{\mathrm{e,UHPC}} \\
& + \kappa^{\mathrm{UHPC}}\langle\mathrm{tr}\,\boldsymbol{\varepsilon}^{\mathrm{e,UHPC}}\rangle_-\mathbf{I}\,.
\end{aligned}
\qquad (11)
$$

Here, the degradation function $g(q)$ is replaced in Eq. (11) by two different continuous stepwise

linearly approximated degradation functions for UHPC in tension $g^+(q)$ and compression $g^-(q)$, for details see [18]. The desired characteristics of the stress-strain curve in a post critical stress softening region due to evolution of fracture can be achieved by calibrating degradation functions $g^\pm(q)$ and parameter ζ, see [14, 19]. The stress tensor $\boldsymbol{\sigma}^{\mathrm{F}}$ for fiber can be calculated as

$$\boldsymbol{\sigma}^{\mathrm{F}} := \sigma^{\mathrm{F}} \boldsymbol{a} \otimes \boldsymbol{a}, \quad (12)$$

using a stress σ^{F} in a preferred direction $\boldsymbol{a}$ reads

$$\sigma^{\mathrm{F}} = E^{\mathrm{F}} \left(e^{\mathrm{F}} - e^{\mathrm{p,F}} \right). \quad (13)$$

The derivation of energy function ψ^{UHPC} for UHPC phase with respect to the phase-field parameter q gives the evolution equation for the phase-field parameter q which reads

$$q - l^2 \operatorname{Div}(\nabla q) - (1-q) \zeta \, \mathcal{H}^{\mathrm{UHPC}} = 0, \quad (14)$$

where the degradation function $g(q) = (1-q)^2$ is considered to ensure an upper bound of the phase-field parameter $q \in [0, 1]$, cf. [12, 15, 19]. A local history field function $\mathcal{H}^{\mathrm{UHPC}}$ is constructed to ensures irreversibility of crack evolution, cf. [14], i.e.,

$$\mathcal{H}^{\mathrm{UHPC}} := \max_{s \in [0,t]} \mathcal{H}_0^{\mathrm{UHPC}}(\mathbf{x}, \tilde{t}) \geq 0 \text{ with}$$

$$\mathcal{H}_0^{\mathrm{UHPC}} = \left\langle \frac{\mathrm{v}^{\mathrm{UHPC}}[\psi_0^{\mathrm{e+,UHPC}} + \psi_0^{\mathrm{p,UHPC}}]}{\psi^{\mathrm{c,UHPC}}} - 1 \right\rangle \quad (15)$$

which is weighted by the volume fraction $\mathrm{v}^{\mathrm{UHPC}}$ for UHPC phase. The use of two different parameters for the critical fracture energies, i.e. $\psi_{\mathrm{t}}^{\mathrm{c,UHPC}}$ and $\psi_{\mathrm{c}}^{\mathrm{c,UHPC}}$, and the degradation functions for UHPC, i.e. $g^+(q)$ and $g^-(q)$, enable the model to capture the distinct behavior of concrete in tension and compression. The sign of the first invariant $\operatorname{tr} \boldsymbol{\sigma}^{\mathrm{UHPC}}$ of the stress tensor for UHPC phase is used to differentiate the critical fracture energies and degradation function in tension and compression, see [18,19]. The non-associative Drucker-Prager yield criterion $\phi_{\mathrm{p}}^{\mathrm{UHPC}}$ is used for UHPC phase which facilitates the modeling of non-linear as well as distinct tension-compression material behavior of concrete, i.e.,

$$\phi_{\mathrm{p}}^{\mathrm{UHPC}} = \frac{1}{\sqrt{2}} ||\operatorname{dev}\boldsymbol{\sigma}_0^{\mathrm{UHPC}}|| - \beta_{\mathrm{p}}\operatorname{tr}\boldsymbol{\sigma}_0^{\mathrm{UHPC}}$$
$$- \left(y_0^{\mathrm{UHPC}} + h^{\mathrm{UHPC}}\alpha^{\mathrm{UHPC}} \right), \quad (16)$$

and a plastic potential $\phi_{\mathrm{n}}^{\mathrm{UHPC}}$ for UHPC phase reads

$$\phi_{\mathrm{n}}^{\mathrm{UHPC}} = \frac{1}{\sqrt{2}} ||\operatorname{dev}\boldsymbol{\sigma}_0^{\mathrm{UHPC}}|| - \beta_{\mathrm{n}}\operatorname{tr}\boldsymbol{\sigma}_0^{\mathrm{UHPC}}, \quad (17)$$

where β_{p} and β_{n} are the material parameters. The evolution equations of plastic strains $\dot{\boldsymbol{\varepsilon}}^{\mathrm{p,UHPC}}$ and the equivalent plastic strain $\dot{\alpha}^{\mathrm{UHPC}}$ for UHPC phase can be calculated, respectively as,

$$\dot{\boldsymbol{\varepsilon}}^{\mathrm{p,UHPC}} = \lambda^{\mathrm{p,UHPC}} \frac{\partial \phi_{\mathrm{n}}^{\mathrm{UHPC}}}{\partial \boldsymbol{\sigma}_0^{\mathrm{UHPC}}} \quad \text{and}$$

$$\dot{\alpha}^{\mathrm{UHPC}} = \lambda^{\mathrm{p,UHPC}}, \quad (18)$$

using the incremental plastic consistency parameter $\lambda^{\mathrm{p,UHPC}}$. For the non-linear behavior along the preferred fiber direction one-dimensional von Mises yield criterion is used, i.e.,

$$\phi^{\mathrm{F}} \left(\sigma^{\mathrm{F}}, \kappa_{\mathrm{p}}^{\mathrm{F}} \right) = |\sigma^{\mathrm{F}}| - \left(y_0^{\mathrm{F}} + h^{\mathrm{F}}\alpha^{\mathrm{F}} \right). \quad (19)$$

The equations for the evolution of a plastic strain $\dot{e}^{\mathrm{p,F}}$ and the equivalent plastic strain $\dot{\alpha}^{\mathrm{F}}$ for fiber are formulated using the incremental plastic consistency parameter $\lambda^{\mathrm{p,F}}$, respectively as,

$$\dot{e}^{\mathrm{p,F}} = \lambda^{\mathrm{p,F}} \frac{\partial \phi^{\mathrm{F}}}{\partial \sigma^{\mathrm{F}}} \quad \text{and} \quad \dot{\alpha}^{\mathrm{F}} = \lambda^{\mathrm{p,F}}. \quad (20)$$

The presented numerical model is implemented in the framework of the finite element method. Therein, the balance of linear momentum using the total stress tensor, see Eq. (10) and the governing equation for the phase-field parameter q, i.e, Eq. (14), are solved using the algorithmic decoupling method described in [15] and solution strategy adopted from [4].

5

4 Numerical calibration and experimental validation

At first, to calibrate the material parameters of UHPC the uniaxial cyclic tension and uniaxial cyclic compression tests of pure UHPC are simulated using the presented numerical model. A cube consisting of pure UHPC, i.e. without embedded fibers, is considered for the simulations. The boundary conditions for uniaxial cyclic tensile and compression tests are shown in Fig. 5a and Fig. 6a, respectively.

The calibrated bases for the interpolation of degradation functions for UHPC in tension $g^+(q)$ and for UHPC in compression $g^-(q)$ are taken from [9, 18]. The experimentally determined mechanical properties of reference mixture of UHPC used for the simulations are listed in Table 2, taken from [13].
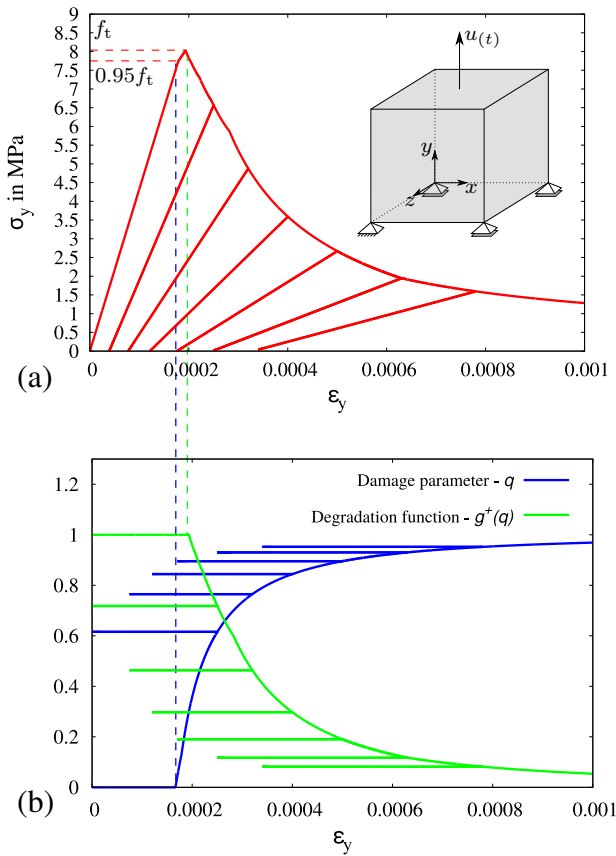
Figure 5: Uniaxial cyclic tensile test of UHPC: (a) stress–strain diagram and (b) evolution of degradation function $g^+(q)$ with respect to the phase-field parameter q.

In this step, initial yield stress y_0^{UHPC}, the Drucker–Prager parameters β_{p} and β_{n}, the hard-

ening parameter h^{UHPC} and the values of critical fracture energies in tension $\psi_{\mathrm{t}}^{\mathrm{c,UHPC}}$ and compression $\psi_{\mathrm{c}}^{\mathrm{c,UHPC}}$ are calibrated using the procedure explained in [18]. The resulting calibrated material parameters are listed in Table 2.
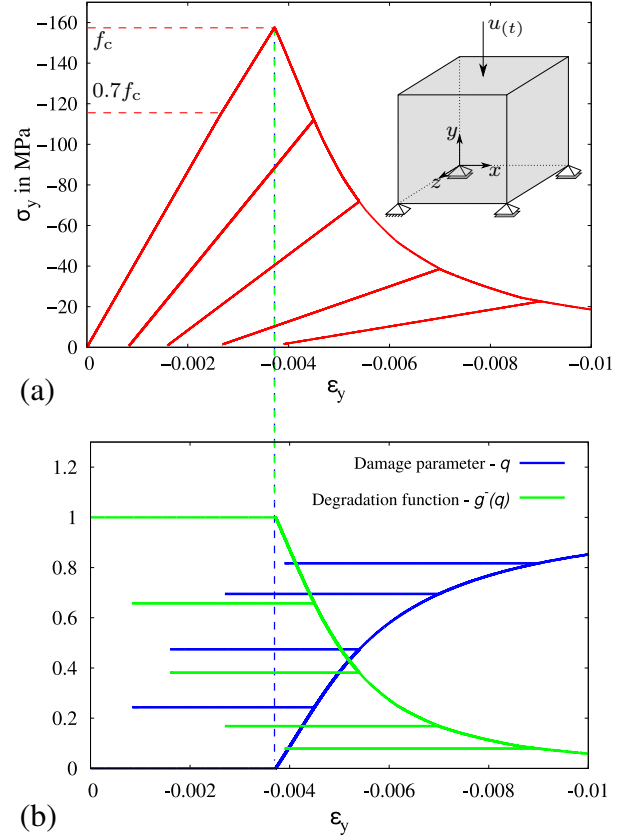
Figure 6: Uniaxial cyclic compression test of UHPC (a) stress–strain diagram and (b) evolution of degradation function $g^-(q)$ with respect to the phase-field parameter q.

The resulting stress–strain characteristic for cyclic tensile and compression tests are shown in Fig. 5a and Fig. 6a, respectively. Therein, the onset of damage occur at $\sigma_y = f_{\mathrm{t}}^{\mathrm{UHPC}}$ in tension test and at $\sigma_y = f_{\mathrm{c}}^{\mathrm{UHPC}}$ in compression test. Note that, this numerical approach is unable to capture the damage that occurs prior to the stress reaching the levels of tensile and compressive strengths, e.g., in case of a sustained loading. Moreover, the yielding start at value of tensile stress $\sigma_y = 0.95 f_{\mathrm{t}}$ in tension test and at the value of compressive stress $\sigma_y = 0.7 f_{\mathrm{c}}$ in compression test, see Fig. 5a and Fig. 6a. The evolution of degradation functions for UHPC in tension $g^+(q)$ and for UHPC in compression

$g^-(q)$ with respect to the phase-field parameter q for uniaxial cyclic tensile and compression tests are shown in Figs. 5b and 6b, respectively.

Table 2: Mechanical properties of UHPC mixture, cf. [13] and calibrated material parameters for UHPC phase, cf. [17].

Parameter	UHPC	unit
E^{UHPC}	43.3	GPa
ν^{UHPC}	0.221	–
$f_{\mathrm{t}}^{\mathrm{UHPC}}$	8.2	MPa
$f_{\mathrm{c}}^{\mathrm{UHPC}}$	158	MPa
$\psi_t^{\mathrm{t,UHPC}}$	$6e-4$	MPa
$\psi_t^{\mathrm{c,UHPC}}$	0.235	MPa
y_0^{UHPC}	8.4	MPa
β_{p}	0.5	–
β_{n}	0.02	–
h^{UHPC}	23000	MPa
l	14	mm
ζ	1	–

In the next step, the efficiency of the proposed numerical model is checked by simulating the three-point bending beam tests at low cycle using the beams of pure UHPC without fibers and the reinforced UHPC with embedded steel microfibers considering different fiber contents, distributions and orientations.
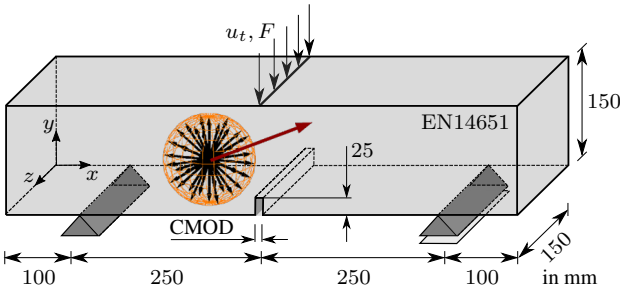
Figure 7: Boundary value problem for three-point bending beam cyclic test with a superimposed ODF containing different distributions and orientations of steel fibers, taken from [9].
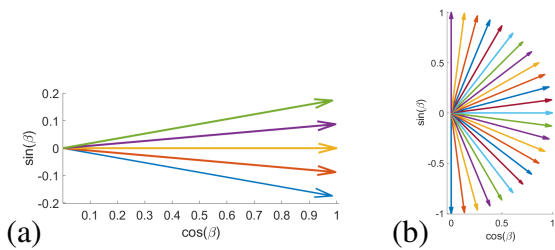
For all these simulations a boundary value problem is constructed according to the European Standard EN 14651. The geometry and boundary conditions for three-point bending beam test are shown in Fig. 7. A vertical displacement boundary condition u_t is applied on the middle of top surface of the beam above the notch. The resulting applied load is calculated by taking the sum of the reaction forces F of constrained nodes at the top surface. The relative displacement of the opposite corners at the bottom of the notch in x-direction is computed to get the values of the CMOD. A plane stress approximation is achieved by using eight noded hexahedral elements and a unit length thickness in z-direction. Thereby, a discretization of the x-y-plane by 3,673 elements is done. The mechanical properties and calibrated material parameter for UHPC phase are taken from Table 2. The calibrated bases for the interpolation of degradation functions $g^+(q)$ and $g^-(q)$ are taken same as for uniaxial tensile and compression tests, see [9, 18]. The material parameters of steel microfibers used for the simulations are taken from [13], see Table 3.

Table 3: Material parameters of steel microfibers used for fiber, taken from [13].

Parameter	Steel fiber	unit
E^{F}	168.5	GPa
v^{F}	0/0.0075/0.015	–
y_0^{F}	3.5758	MPa
h^{F}	1130	MPa

The UHPC beams are simulated separately for three different fiber contents of $0/57/115$ kg/m^3, i.e. the volume percentage of fibers $0/0.75/1.5$ vol.-%. The different fiber content can be applied by changing the value of volume fraction v^{F} for fiber. The simulation of pure UHPC beam is done using the volume fractions $\mathrm{v}^{\mathrm{F}} = 0$ for fiber. For the simulations of reinforced UHPC beam having fiber contents of 57 kg/m^3 and 115 kg/m^3, the values of volume fractions for fiber are taken as $\mathrm{v}^{\mathrm{F}} = 0.0075$ and $\mathrm{v}^{\mathrm{F}} = 0.015$, respectively, see Table 3.
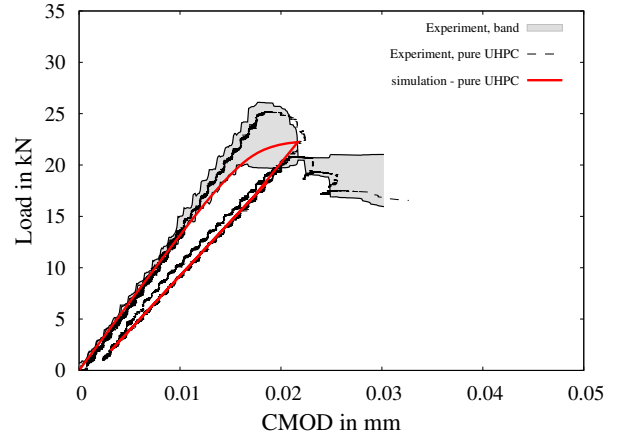
7

To achieve the different fiber orientations and distribution on a beam a superimposed orientation distribution function (ODF) is implemented. The reinforced beam with different fiber contents are simulated using three different fiber orientations. For that purpose the preferred fiber orientations along x-axis is considered as well as an ODF of 5 preferred orientations between the angles -10° to 10° and an ODF of 24 preferred orientations between the angles -90° to 90° are constructed. The ODFs of 5 and 24 preferred orientations are shown in Fig. 8a and Fig. 8b, respectively. The preferred fiber orientations are distributed evenly between the corresponding angles which provides the isotropic distribution of fibers for an ODF of 24 preferred orientations, see Fig. 8b.

tal data, see Fig. 9.

Figure 9: Three-point bending beam test using beam of pure UHPC: comparison of simulated load-CMOD diagramm with experimental data.

The resulting experimental and simulated load-CMOD curves using a reinforced UHPC beam with fiber content of 57 kg/m^3 and 115 kg/m^3 are compared in Figs. 10 and 11, respectively. In these figures the load-CMOD curves for the simulations using different preferred fiber orientations within the reinforced UHPC beams are plotted and compared.

Figure 8: Orientation distribution functions (ODFs) for the steel fibers: (a) of 5 preferred orientations between the angles -10° to 10° and (b) of 24 preferred orientations between the angles -90° to 90° (nearly isotropic), adopted form [9].
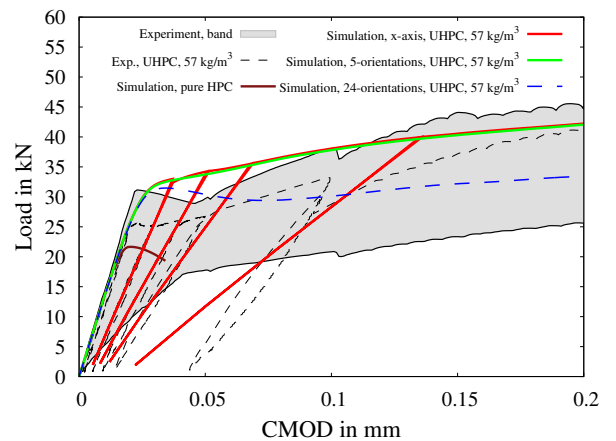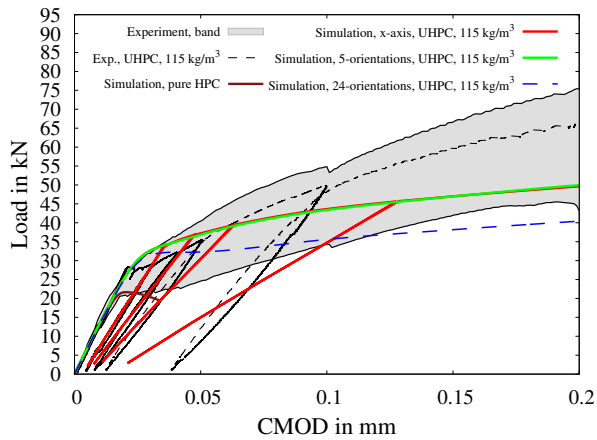
In Figs. 9, 10 and 11, the experimental and simulated load-CMOD curves for fiber content of $0/57/115$ kg/m^3, i.e. $0/0.0075/0.015$ vol. %, are compared, cf. [17]. The experimental data are plotted in terms of a scatter gray band of all experimental load-CMOD curves and a representative experimental load-CMOD curve, see black dotted curve in Figs. 9, 10 and 11. It is observed in the experiment that beam of pure UHPC fails suddenly after the first loading cycle showing strong brittle behavior. For that reason, the three-point bending beam test for pure UHPC is simulated only until the first loading cycle and compared with available experimen-

Figure 10: Three-point bending beam test using fiber-reinforced UHPC with fiber content of 57 kg/m^3: comparison of simulated load-CMOD diagramm with experimental data.

In Figs. 10 and 11, the simulated load-CMOD curves for pure UHPC, see brown curves and reinforced UHPC using a preferred
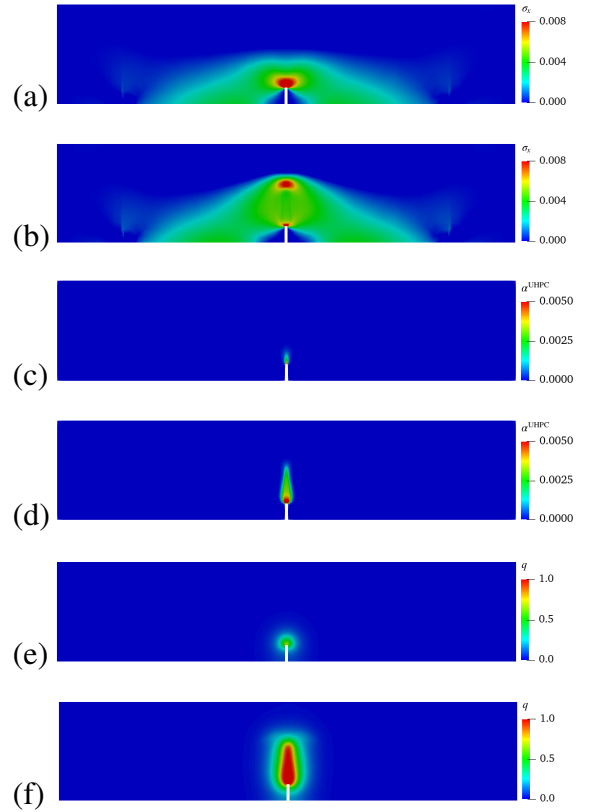
8

fiber direction along x-axis, see red curves, can be considered as upper and lower bounds. The simulated load-CMOD curves using different fiber orientations lie almost within these upper and lower bounds as well as the experimental band showing similar characteristics as observed in the experiments. The simulated load-CMOD curves for reinforced UHPC using an ODF of 5 preferred fiber orientations show similar behavior and same amount of additional stiffness due to reinforced fibers as that of in simulation results using a preferred fiber direction along x-axis, compare red and green curves in Figs. 10 and 11. However, the amount of additional stiffness in simulated load-CMOD curves for reinforced UHPC using ODF of 24 preferred fiber orientations compare to the simulation results using other fiber orientations, see blue dotted curves in Figs. 10 and 11. This is the effect of an isotropic distribution of fibers between the angles -90° to 90°.

Figure 12: Three-point bending beam test at low cycle of reinforced UHPC with fiber content of 57 kg/m^3 and a preferred fiber direction along x-axis: distribution of stress σ_x in x-direction (in GPa), the equivalent plastic strain α^{UHPC} for UHPC phase and the phase-field parameter q for UHPC phase in (a), (c), (e) at CMOD = 0.0232 mm and in (b), (d), (f) at CMOD = 0.107 mm, respectively, cf. [17]

Figure 11: Three-point bending beam test using fiber-reinforced UHPC with fiber content of 115 kg/m^3: comparison of simulated load-CMOD diagramm with experimental data.
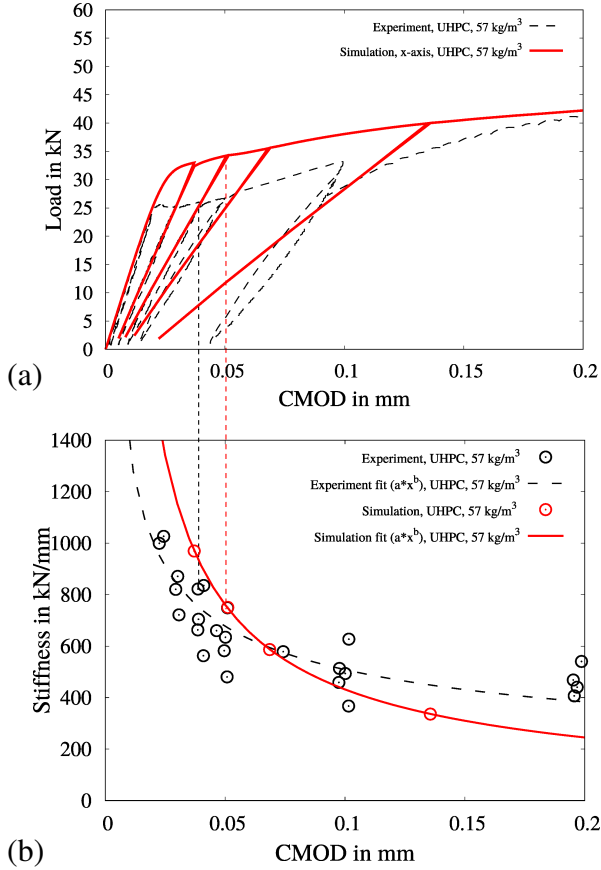
The simulation results for the three-point bending beam test at low cycle of reinforced UHPC with fiber content of 57 kg/m^3 and a preferred fiber direction along x-axis are shown in Fig. 12. Therein, distribution of stress σ_x in x-direction, the equivalent plastic strain α^{UHPC} for UHPC phase and the phase-field parameter q for UHPC phase are plotted.

The procedure explained in Fig. 3 is followed to calculate the residual stiffness of a reinforced beams for the each loading cycle in the load-CMOD curves, for details see [9, 18]. The calculated values of residual stiffness from simulated load-CMOD curves, i.e. red circle and from the all experimental load-CMOD curves, i.e. black circles, are plotted in Figs. 13b and 14b. These values are used to get the interpolated residual stiffness-CMOD experimental and simulated curves, i.e. dotted black curve and solid red curve, respectively. The values of residual stiffness from simulated curves lies well within the scattered experimental residual stiffness values. The comparison of inter-

polated residual stiffness-CMOD curves shows good agreement to validate the capabilities of the proposed model, though they are slightly deviate from each other.

(a)

(b)

Figure 13: Three-point bending beam test at low cycle of reinforced UHPC with fiber content of 57 kg/m³ for a preferred fiber direction along x-axis: comparison of experimental and simulated (a) load-CMOD diagrams and (b) calculated and interpolated residual stiffness-CMOD diagrams.

In Figs. 13a and 14a, the experimental and simulated load-CMOD curves for a three-point bending beam test at low cycle of fiber-reinforced UHPC using a preferred fiber direction along x-axis with fiber content of 57 kg/m³ and 115 kg/m³ are plotted, respectively, to compare with the calculated residual stresses for a each loading unloading cycle. The simulated load-CMOD curves of reinforced UHPC for a preferred fiber direction along x-axis using different fiber contents are compared in Fig. 15.


(a)

(b)
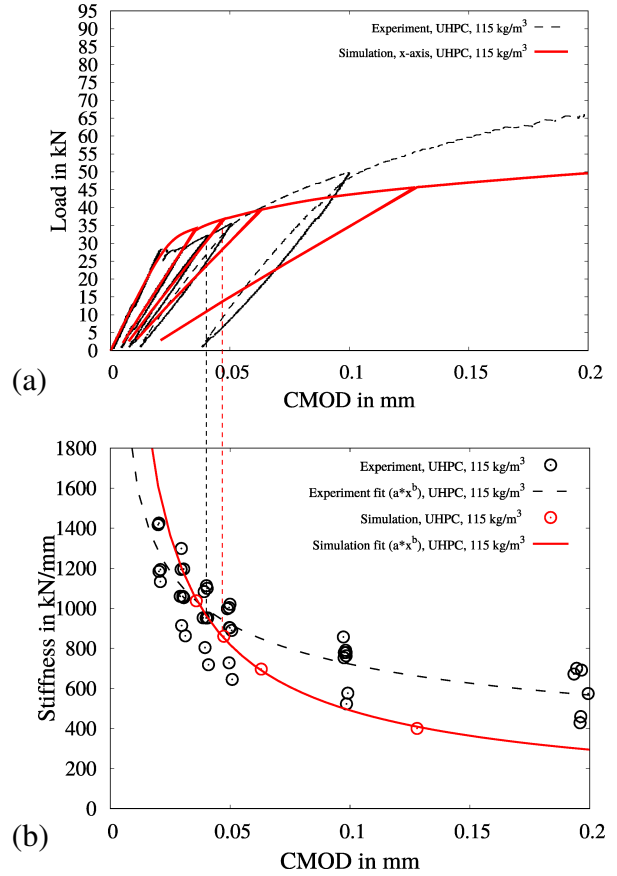
Figure 14: Three-point bending beam test at low cycle of reinforced UHPC with fiber content of 115 kg/m³ for a preferred fiber direction along x-axis: comparison of experimental and simulated (a) load-CMOD diagrams and (b) calculated and interpolated residual stiffness-CMOD diagrams.

5 Conclusion

The three-point bending beam test can be simulated using different fiber contents, orientations and distributions using the presented phenomenological material model. Therein, the fiber contents and fiber orientations can be set just by using the related value of volume fraction for fiber and by implementing the desired superimposed ODF, respectively. The comparison of experimental and simulated load-CMOD curves for the three point bending beam tests for reinforced UHPC shows the ability of the presented model to reproduce the similar failure behavior as observed in the experiments, see Figs. 10 and 11. Furthermore, the presented material model can predict the additional stiffness

10

due to reinforced fibers in beams compared to stiffness for simulation of pure UHPC beams. This additional stiffness increases in the simulation results using the higher volume percentage of reinforced fibers, see Fig. 15.
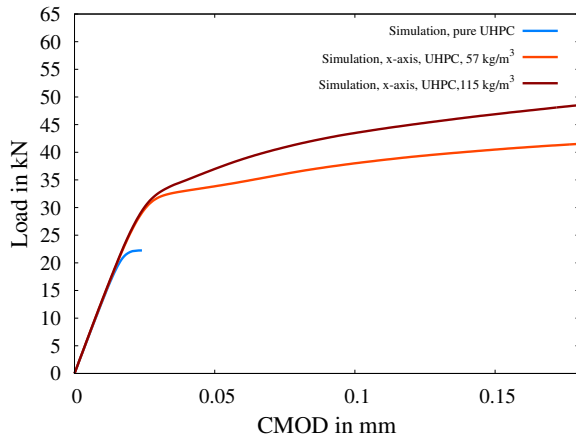
Figure 15: Comparison of simulated load-CMOD diagramms with different fiber contents for a preferred fiber direction along x-axis.

However, the slope of simulated load-CMOD curves for fiber content of 115 kg/m^3 does not match to the slope of the experimental load-COMD curves, see Fig. 11. The calibrations of the bases for degradation functions for UHPC material as well as the interaction between fiber surface to concrete matrix need to be taken into account to improve the prediction capability of numerical model. The simulations using full 3D domain and realistic fiber orientations and distributions are planned in the future to study the overall material behavior of UHPC.

REFERENCES

[1] P. C. Aïtcin. *High-performance concrete.* E & FN Spon, London, 1998.

[2] M. H. Akeed, S. Qaidi, H. U. Ahmed, R. H. Faraj, A. S. Mohammed, W. Emad, B. A. Tayeh, and A. R. G. Azevedo. Ultra-high-performance fiber-reinforced concrete. part i: developments, principles, raw materials. *Case Studies in Construction Materials*, 17:e01290, 2022.

[3] F. Aldakheel. A microscale model for concrete failure in poro-elasto-plastic media. *Theoretical and Applied Fracture Mechanics*, 107:102517, 2020.

[4] M. Ambati, T. Gerasimov, and L. De Lorenzis. Phase-field modeling of ductile fracture. *Computational Mechanics*, 55(5):1017–1040, 2015.

[5] H. Amor, J. J. Marigo, and C. Maurini. Regularized formulation of the variational brittle fracture with unilateral contact: Numerical experiments. *Journal of the Mechanics and Physics of Solids*, 57:1209–1229, 2009.

[6] M. Basaldella, M. Jentsch, N. Oneschkow, M. Markert, and L. Lohaus. Compressive fatigue investigation on high-strength and ultra-high-strength concrete within the spp 2020. *Materials*, 15(11), 2022.

[7] J. P. Boehler. *Applications of tensor functions in solid mechanics*, volume 292. Springer, Vienna, 1987.

[8] G. Gebuhr, S. Anders, M. Pise, D. Brands, and J. Schröder. *Current Perspectives and New Directions in Mechanics, Modelling and Design of Structural Systems: Proceedings of the Eigth International Conference on Structural Engineering, Mechanics and Computation (SEMC 2022), Cape Town, South Africa*, chapter Damage development of steel fibre reinforced high

11

performance concrete in high cycle fatigue tests, pages 1327–1332. CRC Press, Oxon, United Kingdom, 2022.

[9] G. Gebuhr, M. Pise, S. Anders, D. Brands, and J. Schröder. Damage evolution of steel fiber reinforced high performance concrete in low-cycle flexural fatigue: numerical modeling and experimental validation. *Materials*, 15(3):1179, 2022. doi.org/10.3390/ma15031179.

[10] P. Grassl, D. Xenos, U. Nyström, R. Rempling, and K. Gylltoft. A damage-plasticity approach to modelling the failure of concrete. *International Journal of Solids and Structures*, 50:3805–3816, 2013.

[11] J. Grünberg, L. Lohaus, C. Ertel, and M. Wefer. Mehraxiales mechanisches ermüdungsmodell von ultra-hochfestem beton: Experimentelle und analytische untersuchungen. *Beton- und Stahlbetonbau*, 102(6):388–398, 2007.

[12] C. Kuhn, A. Schlüter, and R. Müller. On degradation functions in phase field fracture models. *Computational Materials Science*, 108:374–384, 2015.

[13] J. P. Lanwer, V. Oettel, M. Empelmann, S. Höper, U. Kowalsky, and D. Dinkler. Bond behavior of microsteel fibers embedded in ultra-high performance concrete subjected to monotonic and cyclic loading. *Structural Concrete*, 20:1243–1253, 2019.

[14] C. Miehe, F. Aldakheel, and A. Raina. Phase field modeling of ductile fracture at finite strains: A variational gradient-extended plasticity-damage theory. *International Journal of Plasticity*, 84:1–32, 2016.

[15] C. Miehe, M. Hofacker, and F. Welschinger. A phase field model for rate-independent crack propagation: Robust algorithmic implementation based on operator splits. *Computer Methods*

in Applied Mechanics and Engineering, 199:2765–2778, 2010.

[16] M. Pise, D. Brands, J. Schröder, G. Gebuhr, and S. Anders. Phenomenological material model for damage in steel-fiber reinforced high performance concrete during low cycle fatigue. *Proceedings in Applied Mathematics and Mechanics*, 22(1):e202200236 (6 pages), 2022.

[17] M. Pise, G. Gebuhr, D. Brands, J. Schröder, and S. Anders. Phase-field modeling for failure behavior of reinforced ultra highperformance concrete at low cycle fatigue. *Proceedings in Applied Mathematics and Mechanics*, 2023.

[18] J. Schröder, M. Pise, D. Brands, G. Gebuhr, and S. Anders. Phase-field modeling of fracture in high performance concrete during low-cycle fatigue: numerical calibration and experimental validation. *Computer methods in applied mechanics and engineering*, 398:115181, 2022. doi.org/10.3390/ma15031179.

[19] J. Storm, M. Pise, D. Brands, J. Schröder, and M. Kaliske. A comparative study of micro-mechanical models for fiber pullout behavior of reinforced high performance concrete. *Engineering Fracture Mechanics*, 243:107506, 2021. 10.1016/j.engfracmech.2020.107506.

[20] J. Y. Wu, J. Li, and R. Faria. An energy release rate-based plastic-damage model for concrete. *International Journal of Solids and Structures*, 43:583–612, 2006.

[21] J. Zhang. *Fatigue Fracture of Fibre Reinforced Concrete*. PhD thesis, Technische Universität von Dänemark, 1998.

[22] J. Zhang, J. Li, and J. W. Ju. 3D elasto-plastic damage model for concrete based on novel decomposition of stress. *International Journal of Solids and Structures*, 94–95:125–137, 2016.